



























# Utilizing a Global Network of Telescopes to Update the Ephemeris for the Highly Eccentric Planet HD 80606 b and to Ensure the Efficient Scheduling of JWST

Kyle A. Pearson<sup>1,2</sup> , Charles Beichman<sup>1,3</sup> , B. J. Fulton<sup>3</sup> , Thomas M. Esposito<sup>4,5,6</sup> , Robert T. Zellem<sup>1,2</sup> , David R. Ciardi<sup>3</sup> , Jonah Rolfness<sup>1,2,7</sup>, John Engelke<sup>1,2,8</sup> , Tamim Fatahi<sup>1,2,9</sup> , Rachel Zimmerman-Brachman<sup>1,2</sup>, Arin Avsar<sup>5,6</sup> , Varun Bhalerao<sup>10</sup> , Pat Boyce<sup>2,11</sup>, Marc Bretton<sup>12</sup>, Alexandra D. Burnett<sup>13,14</sup> , Jennifer Burt<sup>1</sup> , Charles H. Cynamon<sup>2,15</sup>, Martin Fowler<sup>2,16</sup>, Daniel Gallego<sup>2</sup>, Edward Gomez<sup>17</sup> , Bruno Guillet<sup>13</sup> , Jerry Hilburn<sup>2</sup>, Yves Jongen<sup>16,18</sup>, Tiffany Kataria<sup>1</sup> , Anastasia Kokori<sup>16,19</sup> , Harsh Kumar<sup>10</sup> , Petri Kuossari<sup>13</sup>, Georgios Lekkas<sup>2,20</sup> , Alessandro Marchini<sup>16,21</sup> , Nicola Meneghelli<sup>13</sup> , Chow-Choong Ngeow<sup>22</sup> , Michael Pimm<sup>13</sup>, Subham Samantaryay<sup>10</sup> , Masao Shimizu (清水正雄)<sup>13</sup>, George Silvus<sup>2,23</sup>, Frank Sienkiewicz<sup>2,24</sup>, Vishwajeet Swain<sup>10</sup> , Joshua Tan<sup>2</sup>, Kalée Tock<sup>2,25</sup>, Kevin Wagner<sup>13,26,27</sup> , and Anaël Wünsche<sup>12,16</sup>

<sup>1</sup> Jet Propulsion Laboratory, California Institute of Technology, Pasadena, CA 91125 USA; [kyle.a.pearson@jpl.nasa.gov](mailto:kyle.a.pearson@jpl.nasa.gov)

<sup>2</sup> Exoplanet Watch, USA

<sup>3</sup> NASA Exoplanet Science Institute, IPAC, California Institute of Technology, Pasadena, CA 91125 USA

<sup>4</sup> SETI Institute, Carl Sagan Center, 339 Bernardo Avenue, Ste 200, Mountain View, CA 94043 USA

<sup>5</sup> Unistellar SAS, 19 Rue Vacon, F-13001 Marseille, France

<sup>6</sup> Department of Astronomy, University of California Berkeley, Berkeley, CA 94720 USA

<sup>7</sup> California Institute of Technology, Pasadena, CA 91125 USA

<sup>8</sup> Raytheon Intelligence, Information, and Services, 300 N Lake Avenue, Suite 1120, Pasadena, CA 91101, USA

<sup>9</sup> Department of Computer Science, California Polytechnic University, San Luis Obispo USA

<sup>10</sup> Department of Physics, Indian Institute of Technology Bombay, Powai, 400076, India

<sup>11</sup> Boyce Research Initiatives and Education Foundation, USA

<sup>12</sup> Observatoire des Baronnies Provençales, Route de Nyons, F-05150 Moydans, France

<sup>13</sup> Unistellar Network Citizen Scientist, USA

<sup>14</sup> School of Natural Resources and the Environment, University of Arizona, Tucson, AZ 85721 USA

<sup>15</sup> SkiesAway Remote Observatory, Bradley, CA, 93426, USA

<sup>16</sup> ExoClock Project, UK

<sup>17</sup> Las Cumbres Observatory, 6740 Cortona Dr, Suite 102, Goleta, CA 93117 USA

<sup>18</sup> Observatoire de Vaison-La-Romaine, Départementale 51, près du Centre Equestre au Palis-F-84110 Vaison-La-Romaine, France

<sup>19</sup> University College London, Gower Street, London, WC1E 6BT, UK

<sup>20</sup> Department of Physics, University of Ioannina, Ioannina, 45110, Greece

<sup>21</sup> University of Siena, Department of Physical Sciences, Earth and Environment, Astronomical Observatory, Via Roma 56, I-53100 Siena, Italy

<sup>22</sup> Graduate Institute of Astronomy, National Central University, 300 Zhongda Road, 32001 Zhongli, Taiwan

<sup>23</sup> American Association of Variable Star Observers, 49 Bay State Road, Cambridge, MA 02138, USA

<sup>24</sup> The Center for Astrophysics, Harvard & Smithsonian, 60 Garden Street, Cambridge, MA 02138, USA

<sup>25</sup> Stanford Online High School, Academy Hall Floor 2 8853, 415 Broadway, Redwood City, CA 94063, USA

<sup>26</sup> Department of Astronomy and Steward Observatory, University of Arizona, Tucson, AZ 85721 USA

Received 2022 June 29; revised 2022 August 15; accepted 2022 August 24; published 2022 October 7

## Abstract

The transiting planet HD 80606 b undergoes a 1000 fold increase in insolation during its 111 days orbit due to it being highly eccentric ( $e = 0.93$ ). The planet's effective temperature increases from 400 to over 1400 K in a few hours as it makes a rapid passage to within 0.03 au of its host star during periapsis. Spectroscopic observations during the eclipse (which is conveniently oriented a few hours before periapsis) of HD 80606 b with the James Webb Space Telescope (JWST) are poised to exploit this highly variable environment to study a wide variety of atmospheric properties, including composition, chemical and dynamical timescales, and large scale atmospheric motions. Critical to planning and interpreting these observations is an accurate knowledge of the planet's orbit. We report on observations of two full-transit events: 2020 February 7 as observed by the TESS spacecraft and 2021 December 7–8 as observed with a worldwide network of small telescopes. We also report new radial velocity observations which, when analyzed with a coupled model to the transits, greatly improves the planet's orbital ephemeris. Our new orbit solution reduces the uncertainty in the transit and eclipse timing of the JWST era from tens of minutes to a few minutes. When combined with the planned JWST observations, this new precision may be adequate to look for non-Keplerian effects in the orbit of HD 80606 b.

*Unified Astronomy Thesaurus concepts:* Exoplanets (498); Observational astronomy (1145); Orbit determination (1175)

*Supporting material:* machine-readable table

<sup>27</sup> NASA Hubble Fellowship Program—Sagan Fellow.

## 1. Introduction

For many years HD 80606 b held the record for the most highly eccentric planet. Discovered by the radial velocity (RV) technique in 2001 (Naef et al. 2001) HD 80606 b has a mass of  $4.1 M_J$ , an orbital period of 111.4 days and an eccentricity of

$\epsilon = 0.93$ . Its eccentricity is currently exceeded only by HD 20782 b with an eccentricity of  $\epsilon = 0.95$  (Jones et al. 2006). HD 80606 b continues to be compelling for further study as it was discovered by Spitzer using the eclipse in early 2009 (Laughlin et al. 2009). The transit was then discovered and announced near-simultaneously in late 2009 February by Fossey et al. (2009), Garcia-Melendo & McCullough (2009), and by Moutou et al. (2009). HD 80606 b passes within 0.03 au of its host G5V star, during its rapid periastron passage of a few tens of hours, the insolation and temperature of the planet increase dramatically, from  $1\times$  to almost  $1000\times$  Earth-equivalent and from 400 to over 1400 K.

These rapid changes, coupled with the fact that HD 80606 b transits and also eclipses (passes behind the star) provide a unique opportunity to explore the dynamical response of an atmosphere under an extreme external forcing function. Spitzer’s photometric observations of eclipses in 2009 and 2010 at 8.0 and 4.5  $\mu\text{m}$ , respectively, were used to infer timescales for radiative, dynamical, and chemical processes (de Wit et al. 2016; Lewis et al. 2017). As noted by Lewis et al. (2017), “The time-variable forcing experienced by exoplanets on eccentric orbits provides a unique and important window on radiative, dynamical, and chemical processes in planetary atmospheres and an important link between exoplanet observations and theory.”

The James Webb Space Telescope (JWST) will expand these studies dramatically using spectroscopy. Kataria et al.<sup>28</sup> will use the MIRI low-resolution spectrometer (MIRI/LRS) to observe an eclipse of HD 80606 b from 5 to 14  $\mu\text{m}$  at a spectral resolution of  $\sim 100$ . Sikora et al.<sup>29</sup> will explore the formation and evolution of atmospheric clouds at shorter wavelengths using NIRSpec at 2.87–5.18  $\mu\text{m}$  with a resolution of  $\sim 2700$  to observe the eclipse and periastron passage. These spectral regions contain a wealth of molecular features whose variation will reveal new insights into the chemistry and dynamics of the atmospheres of giant planets.

A challenge to transit and eclipse observations is the gradual erosion of our knowledge of a planet’s orbital properties. Uncertainties in the timing of transits and eclipses lead to observing inefficiencies as longer durations must be scheduled to avoid missing some or all of an event (e.g., Dragomir et al. 2020; Zellem et al. 2020). This problem is exacerbated in the case of HD 80606 b where the relevant observations are over a decade old and uncertainties on the eclipse prediction grow with each orbit (about three per year). Of particular importance is the knowledge of the time of periastron passage relative to the eclipse as this is needed to link the spectral observations to the insolation profile.

It was to remedy this growing uncertainty in our knowledge of the ephemerides of HD 80606 b that we undertook to analyze the Transiting Exoplanet Survey Satellite (TESS) data and to obtain observations of the transit occurring on 2021 December 7/8 (Table 1 and Figure 2) from the ground. We also obtained new RV measurements around the time of periastron to continue to refine the RV solution. Section 2.2 describes the observations of the transit, and Section 2.4 the

**Table 1**  
Orbital Prior for HD 80606 b

Parameter	Value	Reference
$T_{\text{mid}}$ (MJD)	$2455210.6428 \pm 0.001$	Bonomo et al. (2017)
$E_{\text{mid}}$ (MJD)	$2454424.736 \pm 0.003$	Laughlin et al. (2009)
	14-Jan-2010 0326 UTC	
Period (d)	$111.43670 \pm 0.0004$	Bonomo et al. (2017)
Eccentricity ( $e$ )	$0.93226 \pm 0.00066$	Bonomo et al. (2017)
Arg. Periastris ( $\omega_{\text{peri}}$ )	$58.97 \pm 0.2$ (deg)	Bonomo et al. (2017)
	$-1.0292 \pm 0.0035$ (rad)	
Transit Duration (hr)	$11.64 \pm 0.25$	Winn et al. (2009)
Prediction for Dec. 2021		
Accum. Unc. (hr) <sup>a</sup>	0.4 for Observed transit	
$T_{\text{mid}}$ (MJD)	$2459556.674 \pm 0.016$ d	
Observed event	8-12-2021 0411 UTC	

**Note.**

<sup>a</sup> Accumulated uncertainty in the timing of the transit occurring  $N_{\text{per}} = 39$  periods after the reference time,  $T_c$ .  $\sigma T = \sqrt{\sigma(T_c)^2 + N_{\text{per}}^2 \sigma(\text{Period})^2}$  (Equation (2) in Zellem et al. 2020).

RV observations. Section 3 describes the analysis of the various data sets, while Section 4 uses the combined transit and RV measurements to refine the ephemeris of HD 80606 b and to predict the times of occurrence of future transits and eclipses.

## 2. Observations

A majority of the transit observations for HD 80606 b originated almost a decade ago when it was targeted by the Spitzer Space Telescope. Since then, there hasn’t been a full-transit observation in  $\sim 10$  yr, although the star has been monitored by radial velocity surveys. In preparation for JWST observations we have combined observations of the 2020 transit taken by TESS with 2021 observations taken from the ground by the Exoplanet Watch program. Finally, the light-curve measurements are combined with new and archival radial velocity measurements in order to constrain the orbit parameters and to improve our knowledge of transit and eclipse events over the next decade.

### 2.1. 2020 Transit With TESS

The TESS is conducting an all-sky photometric survey to discover hundreds of transiting planets around bright stars that are most suitable for mass measurements through RV observations (Ricker et al. 2015). TESS acquires observations on a 30-minute cadence of all objects in the field of view but increases the cadence for select bright stars with the goal of detecting small transiting planets (Stassun et al. 2017). The photometric data of HD 80606 from TESS were processed using a custom pipeline leveraging optimal aperture selection, systematic detrending with a weighted spline, and outlier rejection in order to improve and minimize the scatter in the light curve (Pearson 2019). The custom pipeline uses multiple aperture sizes during the photometric extraction in order to minimize the scatter in the residuals after fitting a light-curve model. Detrending the time series and minimizing scatter in the residuals has been shown to improve light-curve quality compared to the default produced from the Science Processing Operations Center (SPOC) pipeline (Jenkins et al. 2016), which is based on the Kepler mission pipeline (Jenkins et al. 2010).

<sup>28</sup> Approved Cycle 1 program #2008. “A Blast From the Past: A Spectroscopic look at the Flash Heating of HD 80606 b” <https://www.stsci.edu/jwst/science-execution/program-information.html?id=2008>.

<sup>29</sup> Approved Cycle 1 program #2488. “Real Time Exoplanet Meteorology: Direct Measurement of Cloud Dynamics on the High-Eccentricity Hot Jupiter HD 80606 b” <https://www.stsci.edu/jwst/science-execution/program-information.html?id=2488>.

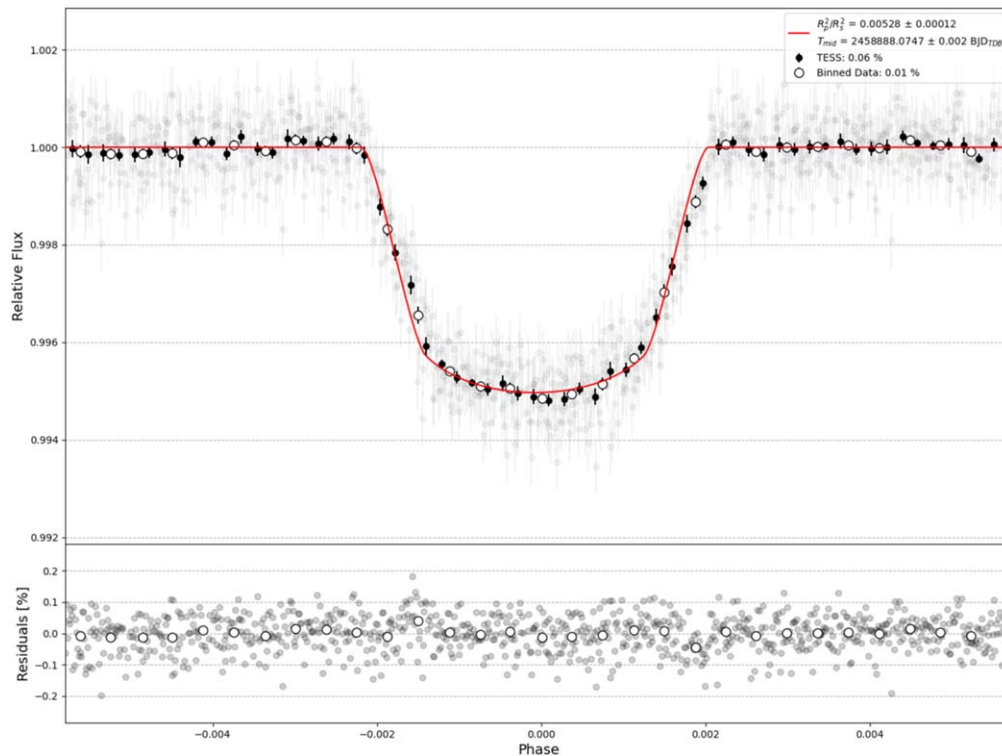


**Figure 1.** A transit light curve of HD 80606 b measured with the TESS spacecraft using data from Sector 21. The TESS light curve is contaminated with light from a neighboring star causing the transit depth to appear smaller (by about  $\sim 48\%$ ) than it really is. The plate scale of TESS is  $\sim 21'' \times 21''$  and that is also coincidentally the distance between the nearby stellar companion, HD 80607, and HD 80606. Light contamination from the roughly equal brightness companion was summed in the aperture used for TESS photometry and will contribute to a smaller measured depth than observations from platforms with a higher imaging resolution, where the light sources can be treated separately. Despite the contamination shrinking the measured depth, we can still detect it to  $\sim 44\sigma$ , which is enough to constrain the time of midtransit to within  $\sim 3$  minutes. The binned data is purely for visualization purposes and is at two different cadences, 30 minutes in black and 60 minutes in white with a black outline, while the transparent points are the original data.

TESS is capable of high precision measurements for this system due to the host star being bright ( $V=9.0$  mag). However, TESS’s large pixel size ( $21''$ ) is less than ideal for HD 80606 due to the presence of HD 80607, a nearby companion of similar spectral type and brightness ( $V=9.07$  mag) separated by  $20''.5$ . Stellar blends dilute the transit signal causing a larger planet to mistakenly appear smaller (e.g., Ciardi et al. 2015; Zellem et al. 2020). In the reduction of TESS data, a wide aperture was used and includes light from both stars. Therefore, our estimate for the transit depth is underestimated. The estimated contamination is around  $\sim 48\%$  and translates to a corrected transit depth  $\sim 2\times$  greater than what we directly measure. Despite the contamination decreasing the transit depth, we still detect the transit at over  $40\sigma$ , which allows for a strong constraint on the time of midtransit to within a few minutes (see Figure 1).

## 2.2. 2021 Transit from the Ground

HD 80606 b’s long transit duration, over 11.5 hr (Pont et al. 2009; Winn et al. 2009), and the accumulated uncertainty in its time of occurrence, make a worldwide program of coordinated observations essential. Fortunately, networks of small and modest-sized telescopes (e.g., Exoplanet Watch,<sup>30</sup> ExoClock,<sup>31</sup> Unistellar<sup>32</sup>) are now in place to support programs of this type. The global observational campaign to measure the 2021



**Figure 2.** A map of the facilities in the global network of small telescopes used to observe the transit on 2021, December 7/8.

December 7–8 transit of HD 80606 b presented here was coordinated by Exoplanet Watch. The various observatories that contributed a transit measurement in December are shown in Figure 2.

### 2.2.1. Exoplanet Watch

Exoplanet Watch is a citizen science project funded by NASA’s Universe of Learning<sup>33</sup> for observing exoplanets with small, ground-based telescopes to maintain ephemerides and to ensure the efficient use of large telescopes, discover new exoplanets via transit timing variations, resolve blended pairs, monitor for stellar variability, and confirm exoplanet candidates

<sup>30</sup> <https://exoplanets.nasa.gov/exoplanet-watch/>

<sup>31</sup> <http://exoclock.space>

<sup>32</sup> <https://unistellaroptics.com/>

<sup>33</sup> <https://www.universe-of-learning.org>

**Table 2**  
Transit Observing Facilities

Facility	Location (N,E)	Size (m)	UTC Start (Phase)	UTC Stop (Phase)	Precision% <sup>a</sup>	N. Images
Transiting Exoplanet Survey Satellite (TESS)	Space	0.1	2020-2-7 20:32:00 (−0.0054)	2020-2-7 07:06:00 (0.0054)	0.06	1520
Exoplanet Watch [HJEB]	(30.7, −104.2)	0.4	2021-12-6 08:21:36 (−0.0166)	2021-12-6 09:40:50 (−0.0161)	1.31	225
Las Cumbres (LCO)	(30.7, −104.2)	0.4	2021-12-7 06:48:56 (−0.0079)	2021-12-7 7:39:54 (−0.0082)	1.26	218
Las Cumbres (LCO)	(30.7, −104.2)	0.4	2021-12-7 09:46:56 (−0.0068)	2021-12-7 10:38:05 (−0.0071)	0.77	225
Las Cumbres (LCO)	(30.7, −104.2)	0.4	2021-12-7 11:35:45 (−0.0064)	2021-12-7 12:26:18 (−0.0061)	1.21	221
Exoplanet Watch [NCC]	(23.5, 120.9)	0.4	2021-12-7 17:34:11 (−0.0042)	2021-12-7 20:13:20 (−0.0032)	1.01	481
GROWTH-India	(32.8, 79.0)	0.7	2021-12-7 19:52:49 (−0.0033)	2021-12-8 00:40:41 (−0.0015)	0.53	609
Unistellar eVscope 2 (2rz)	(49.2, −0.4)	0.11	2021-12-7 20:49:47 (−0.0030)	2021-12-8 01:38:22 (−0.0012)	1.09	126
Unistellar eVscope (etx)	(49.2, −0.4)	0.11	2021-12-7 20:48:29 (−0.0030)	2021-12-8 01:37:27 (−0.0012)	0.63	131
Unistellar eVscope (257)	(60.8, 24.4)	0.11	2021-12-7 21:41:31 (−0.0027)	2021-12-8 00:17:56 (−0.0017)	0.36	79
Unistellar eVscope (3 mh)	(45.3, 11.1)	0.11	2021-12-7 22:24:41 (−0.0024)	2021-12-8 01:41:27 (−0.0012)	0.67	55
Exoplanet Watch [GDAI]	(39.0, −108.2)	0.4	2021-12-8 03:37:37 (−0.0004)	2021-12-8 11:46:49 (0.0026)	3.11	503
Unistellar eVscope (rev)	(30.4, 97.8)	0.11	2021-12-8 04:26:52 (−0.0001)	2021-12-8 08:09:55 (0.0013)	0.50	101
Unistellar eVscope (sdp)	(32.2, −111)	0.11	2021-12-8 05:17:14 (0.0002)	2021-12-8 12:18:15 (0.0028)	0.78	155
Exoplanet Watch [RJBA]	(34.1, −118.1)	0.15	2021-12-8 06:09:47 (0.0005)	2021-12-8 12:08:50 (0.0027)	1.47	569
Exoplanet Watch [CCHD]	(35.8, −120.8)	0.31	2021-12-8 06:13:45 (0.0005)	2021-12-8 09:50:23 (0.0019)	1.51	420
Las Cumbres (LCO)	(30.7, −104.2)	1	2021-12-8 06:41:20 (0.0007)	2021-12-8 12:17:36 (0.0028)	0.33	391
Exoplanet Watch [HJEB]	(30.7, −104.2)	0.4	2021-12-8 06:46:01 (0.0007)	2021-12-8 07:36:43 (0.001)	1.29	225
Las Cumbres (LCO)	(30.7, −104.2)	0.4	2021-12-8 11:35:50 (0.0025)	2021-12-8 12:26:33 (0.0029)	0.80	225
Unistellar eVscope (8 cm)	(35.1, 134.4)	0.11	2021-12-8 13:19:08 (0.0032)	2021-12-8 14:14:42 (0.0035)	1.54	26
Exoplanet Watch [NCC]	(23.5, 120.9)	0.4	2021-12-8 16:04:28 (0.0042)	2021-12-8 20:08:09 (0.0057)	0.80	516
Unistellar eVscope 2 (2rzB)	(49.2, −0.4)	0.11	2021-12-8 21:47:08 (0.0063)	2021-12-8 23:47:48 (0.0071)	1.08	88
Unistellar eVscope (etxB)	(49.2, −0.4)	0.11	2021-12-8 21:48:00 (0.0064)	2021-12-8 23:39:20 (0.007)	1.25	152
Exoplanet Watch [BARO]	(32.6, −116.3)	0.43	2021-12-9 01:26:11 (0.0077)	2021-12-9 01:55:10 (0.0079)	0.97	98
Exoplanet Watch [LGEC]	(28.3, −16.6)	0.4	2021-12-9T02:06:25 (0.008)	2021-12-9 02:15:10 (0.008)	0.80	29
Exoplanet Watch [FMAA]	(31.7, −111.1)	0.15	2021-12-9T04:41:25 (0.009)	2021-12-9 12:06:02 (0.012)	1.79	130

**Note.**

<sup>a</sup> Standard deviation of the residuals. The observations are split between the archival measurements (top) and those taken for the same transit (bottom). For the exoplanet watch observations, the letters in brackets represent the AAVSO Observer code so the data sets can be easily referenced in the future and searchable on their archive.

(Zellem et al. 2019, 2020). Anyone is able to contribute observations to a public data archive,<sup>34</sup> hosted by the American Association of Variable Star Observers,<sup>35</sup> where they are analyzed on a regular basis and used to refine exoplanet ephemerides.<sup>36</sup> The observations listed under Exoplanet Watch in Table 2 are currently available online and are linked to their AAVSO observer code. A majority of the users contributed at least 1 hr of observations using telescopes smaller than 0.5 m. A few notable contributors to the network include the Boyce-Astro Research Observatory (BARO), located at an observing site near Tierra Del Sol and Campo, California. BARO includes a 17 inch telescope and a ZWO ASI 1600 CMOS camera. The observing configuration provides a  $8\frac{1}{3} \times 6\frac{1}{3}$  field of view with a plate scale of  $0\prime\prime.107$  per pixel. Additionally, an individual user was able to capture part of transit egress from the top of the Cahill building on the campus of the California Institute of Technology using a 6 inch telescope and the ASI 224MC camera.

Another contributor is the MicroObservatory which hosts a network of automated remote reflecting telescopes, each with a 6 inch mirror, 560 mm focal length, and KAF1402ME CCD with  $6.8 \mu\text{m}$  sized pixels. With  $2 \times 2$  pixel binning, the image size is  $650 \times 500$  pixels at a pixel scale of approximate  $5\prime\prime \text{px}^{-1}$ . MicroObservatory takes images of exoplanet systems

daily and makes the images publicly available for educational use via their DIY Planet Search program.<sup>37</sup>

### 2.2.2. LCO Network

Las Cumbres Observatory (LCO) is a global telescope network consisting of multiple-meter and submeter-sized telescopes at various locations around the Earth. HD 80606 was observed over the course of 3 days from multiple locations in the LCO network. Unfortunately, weather clouded out most of the Northern Hemisphere so that only a few sites acquired data. A majority of the usable observations come from LCO's telescopes at McDonald Observatory in Texas and Teide Observatory in Tenerife. LCO's 0.4 m telescopes contain SBIG CCD cameras with a field of view  $\sim 29' \times 29'$ , corresponding to a plate scale of  $0\prime\prime.571 \text{ pixel}^{-1}$ . The 1 m telescope apart of LCO contains a Sinistro imager with a  $26' \times 26'$  field of view and a plate scale of  $0\prime\prime.39 \text{ px}^{-1}$ . All of the LCO observations were acquired with the *R* filter, and some observatory-specific details are highlighted in Table 2.

### 2.2.3. Unistellar Network

The Unistellar Network is a global community of citizen scientist observers with Unistellar telescopes who have open access to observing campaigns organized by SETI Institute astronomers, including exoplanet transit observations. Seven

<sup>34</sup> <https://app.aavso.org/exosite/>

<sup>35</sup> <http://aavso.org>

<sup>36</sup> <https://exoplanets.nasa.gov/exoplanet-watch/results/>

<sup>37</sup> <https://mo-www.cfa.harvard.edu/MicroObservatory/>

**Table 3**  
Archival Ephemeris Times

BJD <sub>TDB</sub>	Reference	Status
2454424.736 ± 0.003	Laughlin et al. (2009)	Full Eclipse
2454876.316 ± 0.023	Pont et al. (2009)	Partial Transit
2454876.338 ± 0.017	Kokori et al. (2022)	Partial Transit
2454987.7842 ± 0.0049	Winn et al. (2009)	Full Transit
2455099.196 ± 0.026	Shporer et al. (2010)	Partial Transit
2455210.6420 ± 0.001	Hébrard et al. (2010)	Full Transit
2455210.6502 ± 0.0064	Shporer et al. (2010)	Full Transit
2457439.401 ± 0.012	Kokori et al. (2022)	Partial Transit
2459222.401 ± 0.016	Kokori et al. (2022)	Partial Transit

different eVsopes (“Enhanced Vision Telescopes”) acquired nine observations of HD 80606 b from six different observing locations in North America, Europe, and Japan (Table 2). Of those observations, seven were collected using the Unistellar eVscope 1, which is a 4.5 inch reflecting telescope with a Sony IMX224LQR CMOS sensor at its prime focus. The camera’s field of view is  $37\prime.0 \times 27\prime.7$  with a plate scale of  $1\prime.7 \text{ pixel}^{-1}$ . Individual images had an exposure time of 3.970 s and sensor gain of 2 dB. The two remaining observations were collected using the Unistellar eVscope 2, which shares the design of the eVscope 1 but has a Sony IMX347LQR CMOS sensor. The camera’s field of view is  $45\prime.3 \times 34\prime.0$  with a plate scale of  $1\prime.3 \text{ pixel}^{-1}$ . Individual images had an exposure time of 3.970 s and sensor gain of 0 dB (no digital gain).

#### 2.2.4. ExoClock Project

In addition to the TESS and December transit of HD 80606 b we also report on three additional transit measurements from the project ExoClock (Kokori et al. 2022). The ExoClock project is an open-access citizen science project aimed at conducting transit measurements of exoplanets targeted by the Ariel Mission (Tinetti et al. 2016). The three measurements were taken from ground-based observatories in Europe with midtransit measurements reported in Table 3.

#### 2.2.5. GROWTH

The Global Relay of Observatories Watching Transients Happen (GROWTH) network involves over a dozen institutions dedicated to the follow-up of transient events (Kasliwal et al. 2019). Among these, a number of Asian observatories within the GROWTH collaboration participated in the 2021 December 7/8 campaign, providing critical data during transit ingress. The GROWTH-India Telescope (GIT) is a 0.7 m fully robotic telescope located at the Indian Astronomical Observatory (IAO), Hanle-Ladakh. The telescope is equipped with an Andor Ikon230XL CCD camera which provides a field of view of  $\sim 0.5 \text{ deg}^2$ . GIT observed HD 80606 b for  $\sim 5$  hr on the night of 2022 December 7, obtaining a total of 609 images. The details of the observations are provided in Table 2. Data were reduced following standard procedures, and photometry was performed with EXOTIC as described in Section 2.3

#### 2.3. Transit Data Reduction

Data reduction and calibrations of the individual science images were done by each observer or their group. We encouraged all groups to acquire at least a bias and flat-field frame in order to reduce noise and normalize pixel-to-pixel

changes in sensitivity, respectively. We provided an open-source package for aperture photometry and light-curve fitting in order to make extracting the time series easy and optimal with respect to minimizing sources of noise. The EXOplanet Transit Interpretation Code<sup>38</sup> (EXOTIC; Zellem et al. 2020; T. Fatahi et al. 2022, in preparation) can calibrate images (i.e., bias, flat and dark), plate solves images for better centroiding, and conducts an optimization over comparison star selection and aperture when extracting the photometric time series. After conducting aperture photometry, all of the time series files were combined in order to produce the global light curve shown in Figure 3. The transit light curve code uses limb darkening from Hippke et al. (2019). A mosaic of the individual observations is shown in the Appendix (see Figure 7). The new midtransit times are listed in Table 4.

#### 2.4. Radial Velocity Observations

New radial velocity observations were obtained around periastris in 2021 December using the Levy spectrometer on the 2.4 m Automated Planet Finder telescope (APF; Vogt et al. 2014) and the high-resolution spectrometer (HIRES, on the 10 m Keck I telescope). The new RV measurements are processed using standard data reduction techniques described in Butler et al. (1996). The APF and HIRISE RV values are measured using an Iodine cell-based design in order wavelength calibrate the stellar spectrum. The spectral region from 5000 to 6200 Å is used for measuring the radial velocities. The new observations are listed in Table 5. We used a total of 286 RV measurements spanning 22 yr for the data analysis (see Figure 4) and they are available in a machine-readable format online (see Table 6; Naef et al. 2001; Wittenmyer et al. 2007, 2009; Rosenthal et al. 2021).

### 3. Analysis

The newly acquired data of HD 80606 b along with the historical measurements for RV, transit, and eclipse are analyzed in a self-consistent manner in order to place constraints on the system parameters. The radial velocity observations help constrain the orbit and alignment of HD 80606 b, which is particularly important considering the high eccentricity of the planet can drastically change the transit duration based on the argument of periastron (Hébrard et al. 2010). The transit observations help the size of the planet once the orbit is reliably known and disentangled from degeneracies involving the stellar radius, inclination, and contamination by HD 80607. Additionally, using the measured times of midtransit and mideclipse we can search for deviations from a Keplerian orbit, which is potentially indicative of a companion in the system (Holman & Murray 2005; Nesvorný & Morbidelli 2008).

#### 3.1. Global Light-curve Analysis

Observations for the transit of HD 80606 b on the night of 2021 December 7–8 are combined and fitted simultaneously in order to derive the time of midtransit and radius ratio between the planet and star. Since each observation was acquired at a different location, it requires individual treatment of extinction from Earth’s atmosphere. We adopt a parameterization (e.g., Pearson et al. 2019) which scales exponentially with airmass

<sup>38</sup> <https://github.com/rzellem/EXOTIC>

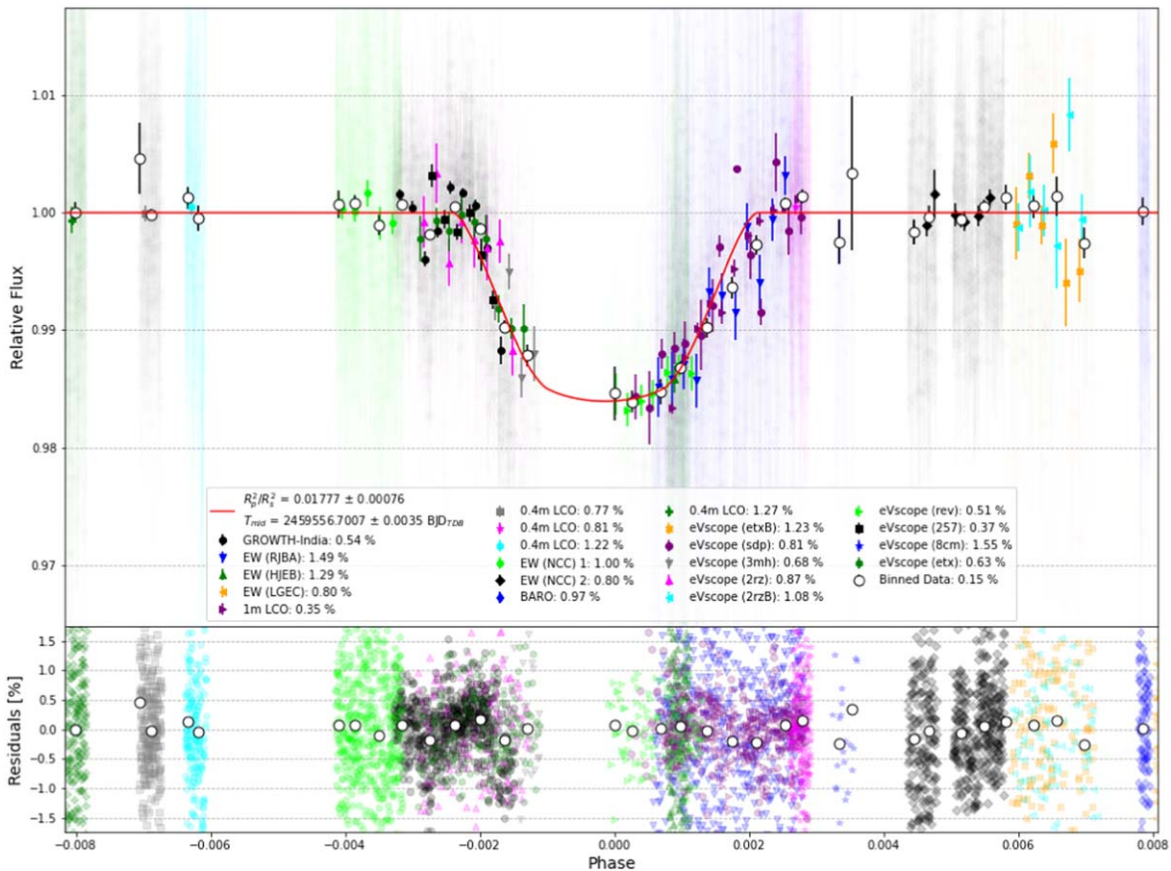


**Figure 3.** Top: the combined light curve showing the complete transit of HD 80606 b on 2021 December 7–8 along with a model fit to the observations (red line). The data are binned to a resolution of 30 minutes for each individual data set and 60 minutes for the combined data set (empty circles) for the purposes of visualization. Each observation is fit simultaneously with Equation (1) and requires a separate airmass model for detrending. A mosaic of individual light curves can be found in the Appendix. Bottom: residuals for the light-curve model are displayed at the native resolution except for a binned version shown in white circles. The standard deviation of the residual scatter is reported in the legend on the top subplot.

**Table 4**  
New Midtransit Times

Facility	BJD <sub>TBD</sub>
TESS	2458888.07466 ± 0.00204
Multiple (7–8 Dec. 2021)	2459556.7007 ± 0.0035

**Table 5**  
New Radial Velocity Observations

Instrument	BJD <sub>TBD</sub>	Relative RV
HIRES	2459514.0886	−133.668 ± 1.168
APF	2459533.0674	37.779 ± 2.332
APF	2459535.9405	15.584 ± 8.951
APF	2459541.0692	−13.924 ± 2.248
APF	2459541.8002	−9.460 ± 2.288
APF	2459544.0027	−28.552 ± 2.413

and has a resemblance to a solution of the radiative transfer equation when  $I(\tau) = I(0)e^{-\tau}$ . The following equation is used to maximize the likelihood of the transit model and airmass signal simultaneously:

$$F_{\text{obs}} = a_0 e^{a_1 \beta} F_{\text{transit}}. \quad (1)$$

Here  $F_{\text{obs}}$  is the flux recorded on the detector,  $F_{\text{transit}}$  is the actual astrophysical signal (i.e., the transit light curve, given by

pyLightcurve (Tsiaras et al. 2016),  $a_i$  are airmass correction coefficients and  $\beta$  is the airmass value. Since the underlying astrophysical signal is shared between all the observations we leave  $R_p/R_s$  and  $T_{\text{mid}}$  as free parameters during the retrieval and share the values between each data set.

The free parameters are optimized using the multimodal nested sampling algorithm called UltraNest (Feroz & Hobson 2008; Buchner 2014; Buchner 2017). UltraNest is a Bayesian inference tool that uses the Monte Carlo strategy of nested sampling to calculate the Bayesian evidence allowing simultaneous parameter estimation and model selection. A nested sampling algorithm is efficient at probing parameter spaces that could potentially contain multiple modes and pronounced degeneracies in high dimensions; a regime in which the convergence for traditional Markov Chain Monte Carlo (MCMC; e.g., Ford 2005) techniques becomes comparatively slow (Skilling 2004; Feroz & Hobson 2008). Convergence for such a large retrieval can take a long time if the priors are very large, and sometimes the solutions will not converge at all within a given range for likelihood evaluations for such a large data set. Therefore, to aid with convergence, each observation was fit individually before being fit simultaneously and given priors to reflect  $\pm 5\sigma$  around the individual fits. The nested sampling algorithm runs for 500,000 likelihood evaluations before terminating with the resulting posterior distribution shown in Figure 8. An open-source version of the global retrieval is available through the EXOTIC

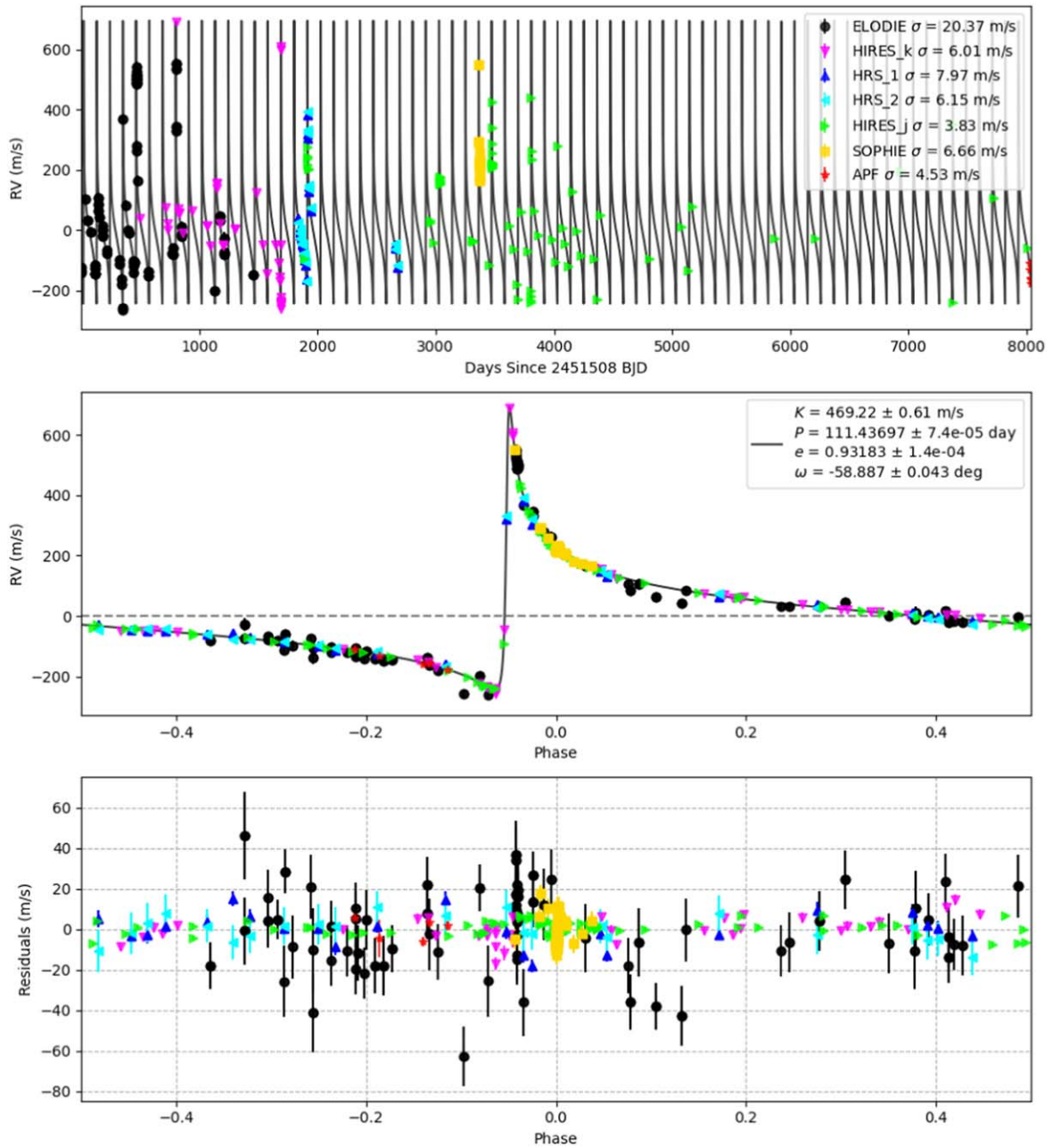


**Figure 4.** Data from 2000 to 2022 show the extremely eccentric orbit of HD 80606 b. The time series RV measurements are plotted in the top panel, the best-fit model is in the middle panel, and the residuals are on the bottom panel. The standard deviation of the residuals is listed in the legend of the top subplot for each data set.

repository on GitHub. see footnote 11 A nonlinear four-parameter limb darkening model is used for both the ground-based measurements and TESS but corresponds to their respective filters (Morello et al. 2020).

### 3.2. Radial Velocity Analysis

The archival and new RV measurements (Table 5 and Table 6) are analyzed using a joint simultaneous fit between a TESS light curve and historical measurements for midtransit and mideclipse in order to constrain a consistent orbital solution across 10 yr of heterogeneous data. The radial velocity model uses the same orbit equation and Keplerian solver as the transit light-curve model (PyLightcurve; Tsiaras et al. 2016).

The orbit equation used in the transit model is

$$r_t = \frac{a}{R_s} \frac{(1 - e^2)}{(1 + e^* \cos(\nu_t))} \quad (2)$$

where  $a$  is the semimajor axis,  $R_s$  is the stellar radius,  $e$  is the eccentricity, and  $\nu$  is the true anomaly at some time  $t$ . The true anomaly can be solved for using Equations (1) and (2) in Fulton et al. (2018) by finding the root of an equation to get the eccentric anomaly which is then used to compute the true anomaly. The orbit equation is projected onto a Cartesian grid that is necessary for the transit model and useful for taking the dot product along our line of sight, ensuring it matches the transit geometry (see Figure 5). The projection along the  $x$ -axis,

**Table 6**  
Archival Radial Velocity Observations

Instrument	BJD <sub>TBD</sub>	Relative RV
ELODIE	2452075.359	-134.46 ± 13
...		
HIRES_K	2452219.162	-85.11 ± 1.6
...		
HRS	2453433.606	119.8 ± 8.6
...		
HIRISE_J	2453398.854	-171.57 ± 0.89
...		
SOPHIE	2454876.729	222.1 ± 5
...		

**Note.** The raw radial velocity measurements (i.e., no relative offset) are available online in a machine-readable format.

(This table is available in its entirety in machine-readable form.)

or our line of sight is

$$x_t = r_t \sin(\nu_t + \omega) \sin(i) \quad (3)$$

where  $i$  is the inclination of the orbit and  $\omega$  is the argument of periastron. The star's velocity is estimated after applying a scaling relation to the planet's orbit, assuming it is in a two-body system. Coupling the orbit solutions ensures a self-consistent system where gravity balances the centripetal acceleration of the planet. The velocity vector of the planet is scaled to match that of the star's orbit and then projected along a line of sight in order to produce the RV signal. A velocity is estimated by evaluating the orbit equation twice in order to compute a numerical derivative using a time step of  $\sim 8.5$  s (0.0001 day):

$$v_{r,t} = \frac{M_p}{M_s} R_s \frac{x_{t+\Delta t} - x_t}{\Delta t}. \quad (4)$$

In addition to scaling the planet's orbit by a mass ratio to mimic the stellar position it must also be scaled by the stellar radius in order to acquire units of meters. The stellar radius is given a Gaussian prior during the retrieval process in order to reflect uncertainties on that scale factor and because it is correlated with the planet's inclination. For instance, for a given transit duration there could be a small star with a noninclined planet or a big star with an inclined planet. Either way, they can produce the same transit duration, and it is difficult to disentangle the two parameters without an additional constraint on the likelihood function (e.g., some spectral modeling is needed to constrain the stellar properties). We do not have enough information to uniquely constrain the stellar radius and inclination simultaneously, which leads to a degeneracy in our retrieval if each parameter uses a uniform prior. Therefore, the stellar radius is given a Gaussian prior that is constructed to be consistent with past derivations in the literature (Bonomo et al. 2017; Rosenthal et al. 2021).

### 3.3. Joint Simultaneous Fit

Fitting three different types of measurements in a joint analysis requires a likelihood function with contributions from each data set. The system parameters are used to generate a coupled physical model for the transit, RV, and ephemeris data in order to enforce consistency between the data sets. The likelihood function includes the sum of the chi-square values

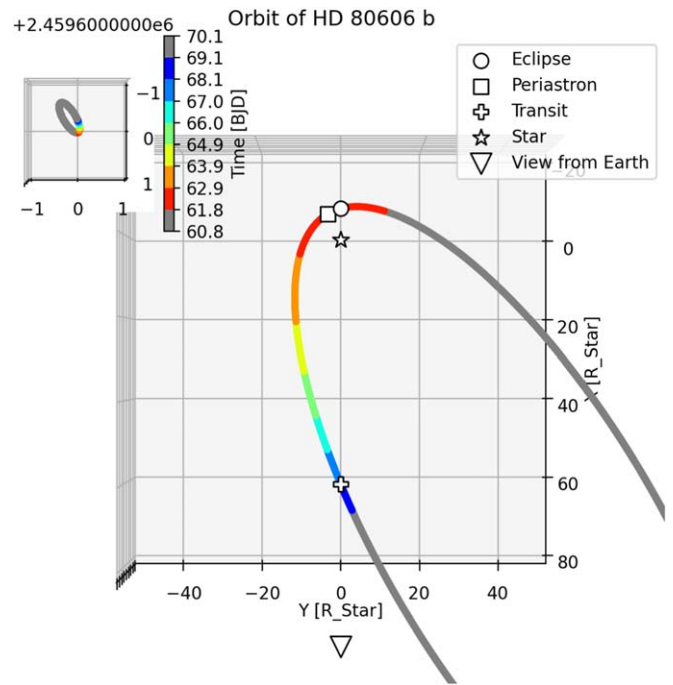


**Figure 5.** Position vectors for the HD 80606 system showing the planet and star plotted over the course of one orbital period for the planet. The colored segments represent chunks of the orbit spanning  $\sim 1$  day. The big plot has a viewing angle  $90^\circ$  above the line of sight. The small subplot also has a top-down view but of the star's orbit. The markers indicate where midtransit, mideclipse, and periastron occur for the planet.

when comparing the data sets to their respective model. The TESS light curve is compared to a transit model in a manner similar to the global fit for all the ground-based measurements, except the airmass correction is left out. The historic midtransit and mideclipse measurements are compared to a linear ephemeris and then folded into the total chi-squared estimate. The radial velocity measurements are also folded into the total chi-squared however the uncertainties are adjusted prior to the joint fit. The radial velocity likelihood ( $\mathcal{L}$ ) adopts a parameterization similar to RADVEL (Fulton et al. 2018) in order to account for underestimated uncertainties,

$$\mathcal{L}_{RV} = -\frac{1}{2} \sum_i \sum_t \left( \frac{d_t - v_{r,t}}{\sigma_{i,t} + \sigma_i} \right)^2, \quad (5)$$

where  $d_t$  is the velocity measurement at time,  $t$ ,  $v_{r,t}$  is the Keplerian model predicted for each RV measurement,  $\sigma_{i,t}$  is the original uncertainty on the radial velocity measurement and  $\sigma_i$  is an RV jitter term for each data set,  $i$ . The jitter term is set after an individual fit to the radial velocity data and before the joint fit. The jitter term scales the uncertainty such that the average uncertainty is roughly equal to the standard deviation of the residuals from the individual fit. Additionally, the solution to the individual fit  $\pm 5\sigma$  is used to constrain the priors for the joint fit. Our uncertainty scaling is similar to RADVEL; however, we do not include a penalty term which is required when fitting for an error scaling term. We adopt an easier correction for underestimated uncertainties while still being able to leverage the optimizations behind nested sampling. The errors are scaled after an individual fit to the RV data such that the average uncertainty is roughly equal to the scatter in the



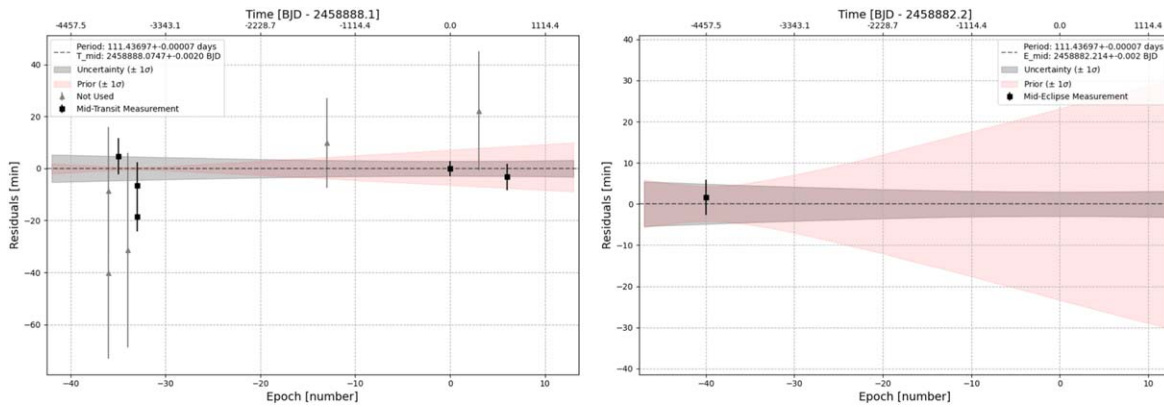


**Figure 6.** left) A comparison of residuals between the measured midtransit times and a calculated linear ephemeris (reported in the plot legend). The gray shaded region indicates the uncertainty in the ephemeris extending to  $\pm 1\sigma$  using our best estimates in Table 7. The pink shaded region indicates an uncertainty based on the prior listed in Table 1. Some midtransit measurements are not used in the joint analysis because they were measured from partial transits. right) An ephemeris estimate for mideclipse times. The pink shaded region shows the uncertainty in a linear solution if we use the Spitzer measurement (Laughlin et al. 2009) as  $E_{mid}$  along with the period from Bonomo et al. (2017). The gray shaded region indicates an uncertainty based on the orbital information listed in Table 7.

residuals for that particular data set. After inflating each uncertainty, we found that our error estimate for the orbital period increased by a factor of  $\sim 2$  and other orbit parameters similarly.

The likelihood function for the joint fit has contributions from transit data, RV measurements, and historic ephemerides using

$$\mathcal{L}_{\text{joint}} = \mathcal{L}_{\text{RV}} + \mathcal{L}_{\text{Transit}} + \mathcal{L}_{\text{Mid-transit}} + \mathcal{L}_{\text{Mid-eclipse}}. \quad (6)$$

The likelihood function for midtransit and mideclipse represent the error for a linear ephemeris estimate compared to existing measurements. Whereas the transit likelihood function uses the photometric time series. Nested sampling is used to efficiently explore a large parameter space defining the system and to build a posterior distribution with which to infer uncertainties (Buchner 2021). The free parameters include the orbital period, time of midtransit, inclination, argument of periastron, eccentricity, a planet mass, and the radius ratio between the planet and star. Posteriors for the free parameters in the joint fit are shown in Figure 9. We also include a Gaussian prior on the stellar radius because it is needed to convert our radial velocity model into meters. The stellar radius is degenerate with inclination, and difficult to constrain if left as a uniform prior. Another relationship in the posteriors is the perfect correlation between eccentricity and argument of periastron. We have seen similar correlations when fitting for  $a_0$  and the RV offset that allowed us to simplify the retrieval and solve for them instead. It is theoretically possible to remove one of these parameters ( $e$  or  $\omega$ ) from the sampling process and solve for the other at runtime without having to build it into the posteriors. That solution however requires solving a transcendental equation on top of the existing orbit solution and would increase the computation time of the likelihood function. Therefore, we include both  $e$  and  $\omega$  in the retrieval and let the sampler handle the correlation, which decreases its efficiency slightly.

#### 4. Results and Conclusions

As part of an effort to refine the orbital ephemeris for HD 80606 b, we have obtained new radial velocity and transit measurements for HD 80606 b. The transit measurements were

obtained with TESS in 2020 and a ground-based campaign in 2021; together, the new data, coupled with archival RV and transit observations, provide a valuable constraint on the time of conjunction. We are able to refine the estimate on the orbital period of HD 80606 b by taking advantage of the 10 yr baseline between the archival and the new observations. Using only the data from 2009 to 2010, the uncertainty on the orbital period was  $\sigma(P) = 4 \times 10^{-4}$ ; combining the old data with the new observations, the new value of the period 111.436971 days has an improved uncertainty of  $\sigma(P) = 7.4 \times 10^{-5}$  days (Figure 6). The period estimate is improved by factor  $\sim 5$  compared to Bonomo et al. (2017) along with significant improvements for the system parameters as summarized in Table 7. The immediate benefit of these new observations is to greatly reduce the uncertainty in the timing of future events (transits or eclipses; e.g., Zellem et al. 2020).

In the case of an eclipse in 2022 November, e.g., in mid-Cycle 1 for JWST, the uncertainty resulting from propagating the ephemeris in Table 1 is  $\sim 24$  minutes, whereas with the new linear ephemeris the uncertainty is  $\sim 5$  minutes (See Figure 6). The linear ephemeris uses the eclipse midpoint from (Laughlin et al. 2009) and our new period estimate. We also provide a more conservative error estimate based on the orbit solution, which yields an uncertainty  $\sim 30$  minutes. The orbit solution has a larger uncertainty than the linear propagation due to the uncertainty in  $e$  and  $\omega$  on the estimated eclipse time. For example, the mideclipse time predicted from the prior is  $2458882.207 \pm 0.10$ , and from our posterior we get  $2458882.214 \pm 0.021$  which leads to a difference in the uncertainty of  $\sim 2$  hr. The errors are significantly larger on predicting mideclipse because of a degeneracy between  $e$  and  $\omega$  and it is exacerbated with larger orbital periods. Removing the degeneracy may be possible by simultaneously fitting a transit and eclipse. The uncertainties reported in Figure 6 are smaller than the ones estimated above because they use a linear propagation of the average orbit solution. It is also important to note that the uncertainty on inclination in the prior does not always yield a transiting planet when conducting a Monte Carlo simulation. Simultaneously fitting a TESS light curve with RV data allowed for a strong constraint on the inclination that helped measure the transit duration to within  $\sim 7$  minutes compared to the full event, which is almost 12 hr.

**Table 7**  
System Parameters for HD 80606

Parameter	Explanation	Our Study	Rosenthal et al. 2021	Bonomo et al. 2017
$M_*$ ( $M_\odot$ )	Stellar Mass	1.05	$1.047 \pm 0.047$	$1.018 \pm 0.035$
$R_*$ ( $R_\odot$ )	Stellar Radius	$1.050 \pm 0.01^a$	$1.066 \pm 0.024$	$1.037 \pm 0.032$
$T_*$ (K)	Stellar Temperature	5565	$5565 \pm 92$	$5574 \pm 72$
Fe/H	Stellar Metallicity	0.35	$0.348 \pm 0.057$	$0.340 \pm 0.050$
$(R_p/R_*)_{\text{contaminated}}$	Planet-Star Radius Ratio	$0.07268 \pm 0.00085$		
$(R_p/R_*)_{\text{contaminated}}^2$	Radius Ratio Squared	$0.00528 \pm 0.00012$		
$(R_p/R_*)_{\text{corrected}}^2$	Radius Ratio Squared	$0.01019 \pm 0.00023^b$		$0.00991 \pm 0.00076$
$R_p$ ( $R_{\text{Jupiter}}$ )	Planet Radius	$1.032 \pm 0.015$		$1.003 \pm 0.023$
$M_p$ ( $M_{\text{Jupiter}}$ )	Planet Mass	$4.1641 \pm 0.0047$	$4.16 \pm 0.13^c$	$4.1 \pm 0.1$
$K$ ( $\text{m s}^{-1}$ )	RV Semiamplitude	$469.22 \pm 0.61$	$465.5 \pm 2.8$	$474.9 \pm 2.6$
Period (day)	Orbital period	$111.436765 \pm 0.000074$	$111.43639 \pm 0.00032$	$111.4367 \pm 0.0004$
$E_{\text{mid}}$ [BJD]	Eclipse Midpoint	$2458882.214 \pm 0.0021^d$		
$E_{14}$ (day)	Eclipse Duration	$0.07169 \pm 0.00073$		
$T_{\text{peri}}$ [BJD]	Epoch of periastron	$2458882.344 \pm 0.0021$		
$T_{\text{mid}}$ [BJD]	Transit Midpoint	$2458888.07466 \pm 0.00204$	$2455099.39 \pm 0.13$	$2455210.6428 \pm 0.001$
$T_{14}$ (day)	Transit Duration	$0.4990 \pm 0.0048$		
$i$ (deg)	Inclination	$89.24 \pm 0.01$		$89.23 \pm 0.3$
$a/R_*$	Scaled Semimajor axis	$94.452 \pm 0.014$	$92.8 \pm 2.5$	$94.6 \pm 3.1$
$a$ (au)	Semimajor axis	$0.4603 \pm 0.0021$	$0.4602 \pm 0.0071$	$0.4565 \pm 0.0053$
$e$	Eccentricity	$0.93183 \pm 0.00014$	$0.93043 \pm 0.00068$	$0.93226 \pm 0.00064$
$\omega$ (deg)	Arg. of periastron	$-58.887 \pm 0.043$	$-58.95 \pm 0.25$	$-58.97 \pm 0.2$

**Notes.** The values in parentheses are calculated using the respective column's orbit solution and a Monte Carlo simulation with 10,000 forward model evaluations.

<sup>a</sup> Gaussian Prior.

<sup>b</sup> Corrected for stellar contamination using brightness values for HD 80606:  $V\text{-mag} = 9.00$  and HD80607:  $V\text{-mag} = 9.07$ .

<sup>c</sup>  $M_p \sin(i)$ .

<sup>d</sup> Uncertainty estimated with fixed  $\omega$ .

For the analysis of the JWST phase curve it is important to know the offset between the eclipse, which will be well determined by the JWST observations, and time of periapsis, which will not be directly measured. The timing of eclipse relative to periapsis depends on three key variables: orbital period  $P$ , eccentricity  $e$ , and argument of periapsis  $\omega$  in Equation (7) (Huber et al. 2017; Alonso 2018):

$$T_{\text{ecl}} - T_{\text{peri}} = \frac{P}{2\pi\sqrt{1-e^2}} \int_0^{-\frac{\pi}{2}-\omega} \left( \frac{1-e^2}{1+e\cos(x)} \right)^2 dx. \quad (7)$$

A Monte Carlo simulation for the parameters with their associated uncertainties (Table 7) yields an offset in time between the eclipse and periapsis of  $\Delta T = -3.104 \pm 0.011$  hr, i.e., with the eclipse occurring before periapsis. This is to be compared with  $-3.069 \pm 0.049$  hr derived using the Bonomo et al. (2017) parameters in Table 1, a difference of  $\sim 2$  minutes. Table 8 takes the times of periapsis, eclipse and conjunction from our solution (Table 7) and propagates these forward in time from 2020 to 2031. The uncertainties include a constant term from the initial Monte Carlo estimates plus the growth in uncertainty occurring  $N$  periods after the reference time.

Finally, we note that the increased precision of the ephemeris, when combined with new JWST observations, may allow an exploration of non-Keplerian effects such as tidal dissipation (Fabrycky 2010) or General Relativistic effects similar to those seen in the precession of the periapsis in orbit of Mercury in our solar system, but greatly enhanced by the high eccentricity of HD 80606 b. Blanchet et al. (2019) calculate that offsets between transit and eclipse midpoints should grow as the number of orbits increases. While the precision and temporal baseline of the 2009–2010 measurements is inadequate to measure the predicted

effects of 3–4 minutes, the high precision expected from JWST's great sensitivity makes such measurements possible over the next few years. Additionally, our measurements reported in this paper will be archived on ExoFOP enabling future studies to search for long-term perturbations that may affect the ephemeris estimates.

Some of the research described in this publication was carried out in part at the Jet Propulsion Laboratory, California Institute of Technology, under a contract with the National Aeronautics and Space Administration. This research has made use of the NASA Exoplanet Archive and ExoFOP, which is operated by the California Institute of Technology, under contract with the National Aeronautics and Space Administration under the Exoplanet Exploration Program.

This publication makes use of data products from Exoplanet Watch, a citizen science project managed by NASA's Jet Propulsion Laboratory on behalf of NASA's Universe of Learning. This work is supported by NASA under award number NNX16AC65A to the Space Telescope Science Institute, in partnership with Caltech/IPAC, the Harvard-Smithsonian Center for Astrophysics, and NASA Jet Propulsion Laboratory.

We acknowledge with thanks the use of the AAVSO Exoplanet Database contributed by observers worldwide and used in this research.

This work makes use of observations from the Las Cumbres Observatory global telescope network. The authors thank Dr. Lisa Storie-Lombardi for the grant of Director's Discretionary Time with the Los Cumbres Observatory (LCO), which was critical to the execution of this program. Dr. Rachel Street helped to identify the appropriate telescopes and observing modes for LCO.

**Table 8**  
Predicted Transit, Eclipse, and Periapsis Times

Period	Periapsis Date	$T_{\text{Peri}}$ (BJD <sub>TDB</sub> )	$E_{\text{mid}}$ (BJD <sub>TDB</sub> )	$T_{\text{mid}}$ (BJD <sub>TDB</sub> )
0	2020-2-2 20:15:10	2458882.344 ± 0.0021	2458882.214 ± 0.0021	2458888.0746 ± 0.0020
1	2020-5-24 06:44:36	2458993.781 ± 0.0021	2458993.651 ± 0.0021	2458999.5116 ± 0.0020
2	2020-9-12 17:14:03	2459105.218 ± 0.0021	2459105.089 ± 0.0021	2459110.9487 ± 0.0020
3	2021-1-2 03:45:18	2459216.656 ± 0.0021	2459216.527 ± 0.0021	2459222.3855 ± 0.0021
4	2021-4-23 14:12:08	2459328.092 ± 0.0021	2459327.962 ± 0.0021	2459333.8225 ± 0.0021
5	2021-8-13 00:42:14	2459439.529 ± 0.0022	2459439.400 ± 0.0022	2459445.2595 ± 0.0022
6	2021-12-2 11:10:00	2459550.965 ± 0.0022	2459550.836 ± 0.0022	2459556.6963 ± 0.0021
7	2022-3-23 21:40:27	2459662.403 ± 0.0021	2459662.274 ± 0.0022	2459668.1333 ± 0.0021
8	2022-7-13 08:09:58	2459773.840 ± 0.0022	2459773.711 ± 0.0021	2459779.5704 ± 0.0021
9	2022-11-1 18:39:52	2459885.278 ± 0.0023	2459885.148 ± 0.0022	2459891.0073 ± 0.0022
10	2023-2-21 05:08:03	2459996.714 ± 0.0022	2459996.584 ± 0.0023	2460002.4443 ± 0.0022
11	2023-6-12 15:37:31	2460108.151 ± 0.0023	2460108.021 ± 0.0021	2460113.8814 ± 0.0022
12	2023-10-2 02:07:17	2460219.588 ± 0.0023	2460219.459 ± 0.0022	2460225.3183 ± 0.0022
13	2024-1-21 12:36:17	2460331.025 ± 0.0022	2460330.896 ± 0.0022	2460336.7554 ± 0.0023
14	2024-5-11 23:06:49	2460442.463 ± 0.0024	2460442.334 ± 0.0023	2460448.1923 ± 0.0023
15	2024-8-31 09:35:05	2460553.899 ± 0.0023	2460553.770 ± 0.0023	2460559.6291 ± 0.0023
16	2024-12-20 20:01:54	2460665.335 ± 0.0023	2460665.205 ± 0.0024	2460671.0663 ± 0.0023
17	2025-4-11 06:33:17	2460776.773 ± 0.0024	2460776.644 ± 0.0024	2460782.5030 ± 0.0023
18	2025-7-31 17:03:20	2460888.211 ± 0.0024	2460888.081 ± 0.0025	2460893.9400 ± 0.0025
19	2025-11-20 03:30:27	2460999.646 ± 0.0025	2460999.517 ± 0.0024	2461005.3771 ± 0.0024
20	2026-3-11 14:00:39	2461111.084 ± 0.0024	2461110.954 ± 0.0024	2461116.8140 ± 0.0025
21	2026-7-1 00:29:17	2461222.520 ± 0.0024	2461222.391 ± 0.0025	2461228.2509 ± 0.0025
22	2026-10-20 10:59:11	2461333.958 ± 0.0026	2461333.828 ± 0.0025	2461339.6880 ± 0.0025
23	2027-2-8 21:26:36	2461445.393 ± 0.0025	2461445.264 ± 0.0026	2461451.1249 ± 0.0026
24	2027-5-31 07:56:26	2461556.831 ± 0.0025	2461556.701 ± 0.0026	2461562.5616 ± 0.0027
25	2027-9-19 18:27:19	2461668.269 ± 0.0026	2461668.140 ± 0.0026	2461673.9988 ± 0.0026
26	2028-1-9 04:54:59	2461779.705 ± 0.0027	2461779.575 ± 0.0027	2461785.4358 ± 0.0027
27	2028-4-29 15:27:05	2461891.144 ± 0.0028	2461891.014 ± 0.0027	2461896.8728 ± 0.0028
28	2028-8-19 01:54:49	2462002.580 ± 0.0028	2462002.450 ± 0.0028	2462008.3097 ± 0.0029
29	2028-12-8 12:23:09	2462114.016 ± 0.0029	2462113.887 ± 0.0029	2462119.7467 ± 0.0030
30	2029-3-29 22:52:37	2462225.453 ± 0.0030	2462225.324 ± 0.0029	2462231.1838 ± 0.0031
31	2029-7-19 09:22:28	2462336.891 ± 0.0030	2462336.761 ± 0.0031	2462342.6207 ± 0.0031
32	2029-11-7 19:51:46	2462448.328 ± 0.0032	2462448.198 ± 0.0030	2462454.0576 ± 0.0030
33	2030-2-27 06:22:46	2462559.766 ± 0.0031	2462559.636 ± 0.0032	2462565.4946 ± 0.0031
34	2030-6-18 16:50:58	2462671.202 ± 0.0032	2462671.072 ± 0.0032	2462676.9315 ± 0.0031
35	2030-10-8 03:19:59	2462782.639 ± 0.0033	2462782.509 ± 0.0033	2462788.3685 ± 0.0032

Some of the data presented herein were obtained at the W. M. Keck Observatory, which is operated as a scientific partnership between the California Institute of Technology, the University of California, and the National Aeronautics and Space Administration. The Observatory was made possible by the generous financial support of the W. M. Keck Foundation. The authors wish to recognize and acknowledge the very significant cultural role and reverence that the summit of Maunakea has always had within the indigenous Hawaiian community. We are most fortunate to have the opportunity to conduct observations from this mountain.

Some of the scientific data presented herein were obtained using the eVscope Network, which is managed jointly by Unistellar and the SETI Institute. The Unistellar Network and work by T.M.E. and A.A. are supported by grants from the Gordon and Betty Moore Foundation. The authors wish to thank Prof. S. Kulkarni for an introduction to members of the GROWTH consortium.

The results reported herein benefited from collaborations and/or information exchange within NASA's Nexus for Exoplanet System Science (NExSS) research coordination network sponsored by NASA's Science Mission Directorate.

K.W. acknowledges support from NASA through the NASA Hubble Fellowship grant HST-HF2-51472.001-A awarded by the Space Telescope Science Institute, which is operated by the

Association of Universities for Research in Astronomy, Incorporated, under NASA contract NAS5-26555.

This research has made use of the NASA Exoplanet Archive, which is operated by the California Institute of Technology, under contract with the National Aeronautics and Space Administration under the Exoplanet Exploration Program.

The ExoClock project has received funding from the UKSA and STFC grants: ST/W00254X/1 and ST/W006960/1.

This work made use of data from the GROWTH-India Telescope (GIT) set up by the Indian Institute of Astrophysics (IIA) and the Indian Institute of Technology Bombay (IITB). It is located at the Indian Astronomical Observatory (Hanle), operated by IIA. We acknowledge funding by the IITB alumni batch of 1994, which partially supports operations of the telescope. Telescope technical details are available at <https://sites.google.com/view/growthindia/>.

This work uses funding from the Ministry of Science and Technology (Taiwan) under contract 109-2112-M-008-014-MY3, and we are thankful for their support. The queue observations were done using the 0.4 m SLT telescope located at the Lulin Observatory, with assistance from observatory staff C.-S. Lin, H.-Y. Hsiao, and W.-J. Hou.

*Facility:* Keck: I (HIRES), Lick: APF, LCO, TESS, Spitzer Space Telescope, Keck Observatory Archive (KOA).

## Appendix

The appendix contains figures regarding the best-fit solution for the ground-based transit light curve (see Figure 7) along with posteriors from the analysis (see Figures 8 and 9).

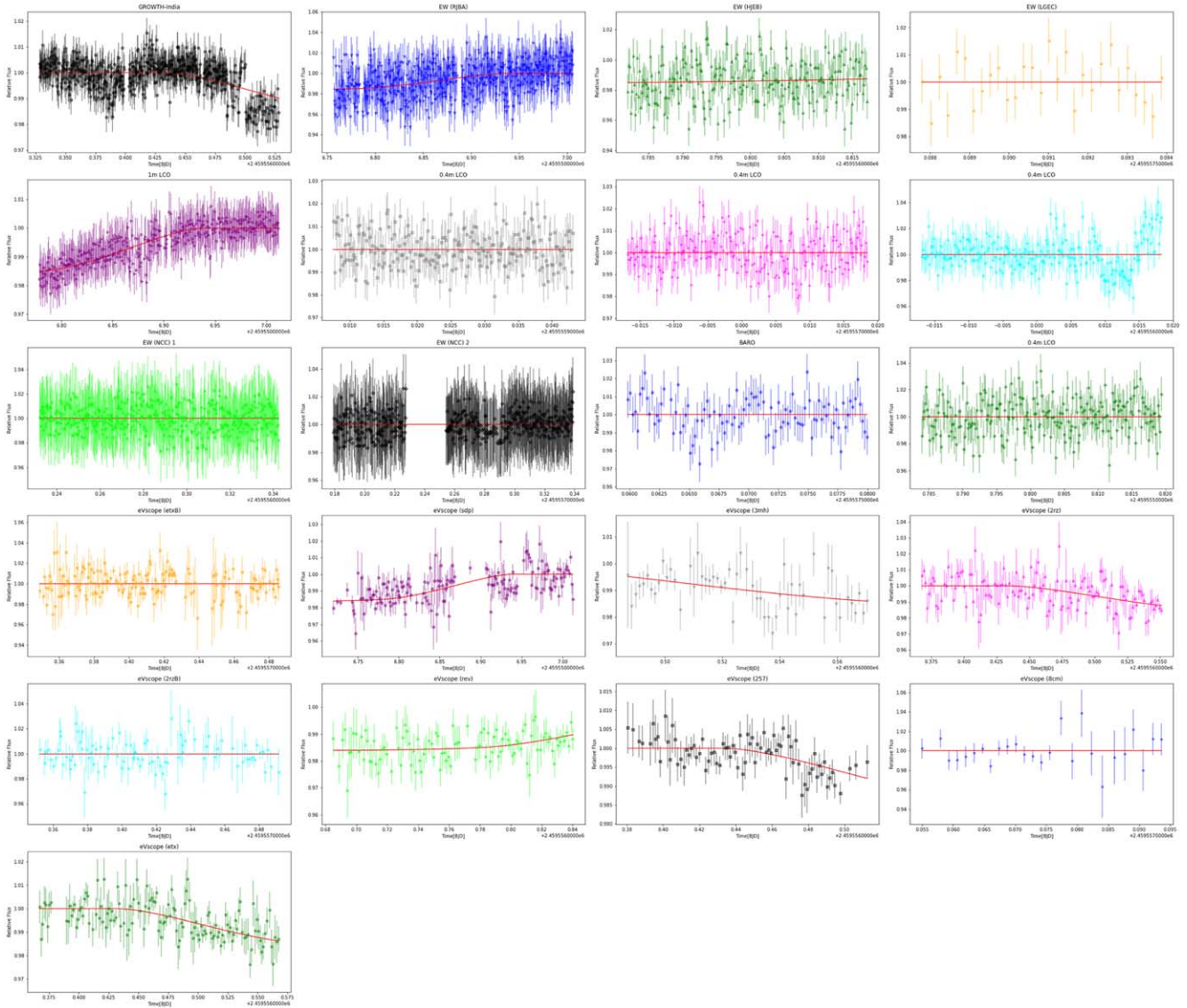


**Figure 7.** A mosaic of observations for the transit of HD 80606 b on the night of 2021 December 7–8. A global light-curve model is overplotted in red. All of these observations are stitched together into a single time series shown in Figure 3.

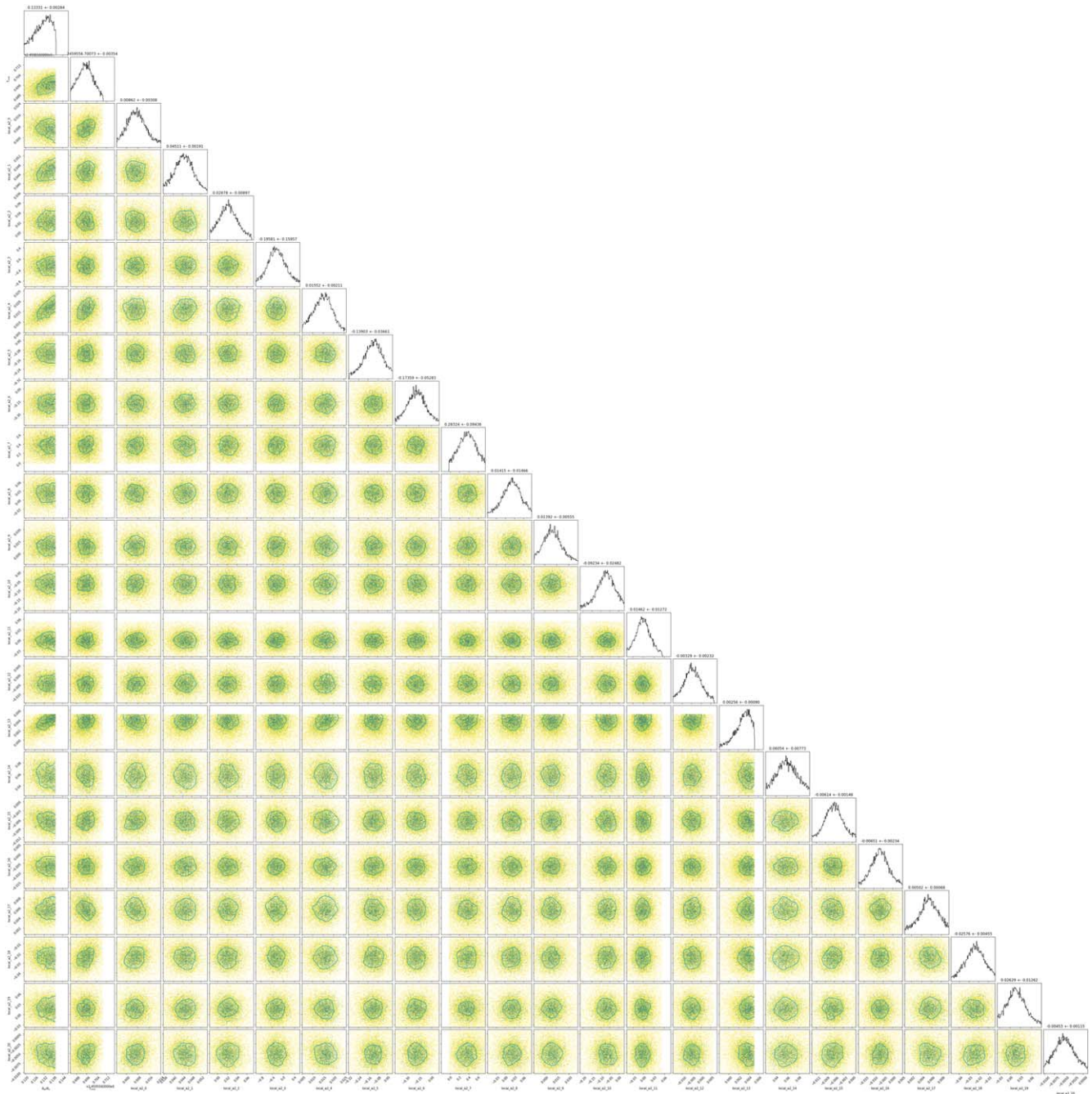


**Figure 8.** Posteriors for the global light-curve solution on 2021 December 7–8. All of the observations shown in Figure 3 are fit simultaneously in order to constrain the time of midtransit and transit depth from a global light-curve model. Each observation was acquired at a different airmass and requires individual treatment in order to detrend properly, and those coefficients make up a majority of this distribution. The data points in each correlation plot are color coded to the likelihood, with darker colors representing higher likelihoods. The contour represents roughly the  $1\sigma$  boundary using the uncertainty reported in each plot’s title. Each value in the prior starts as a uniform distribution.

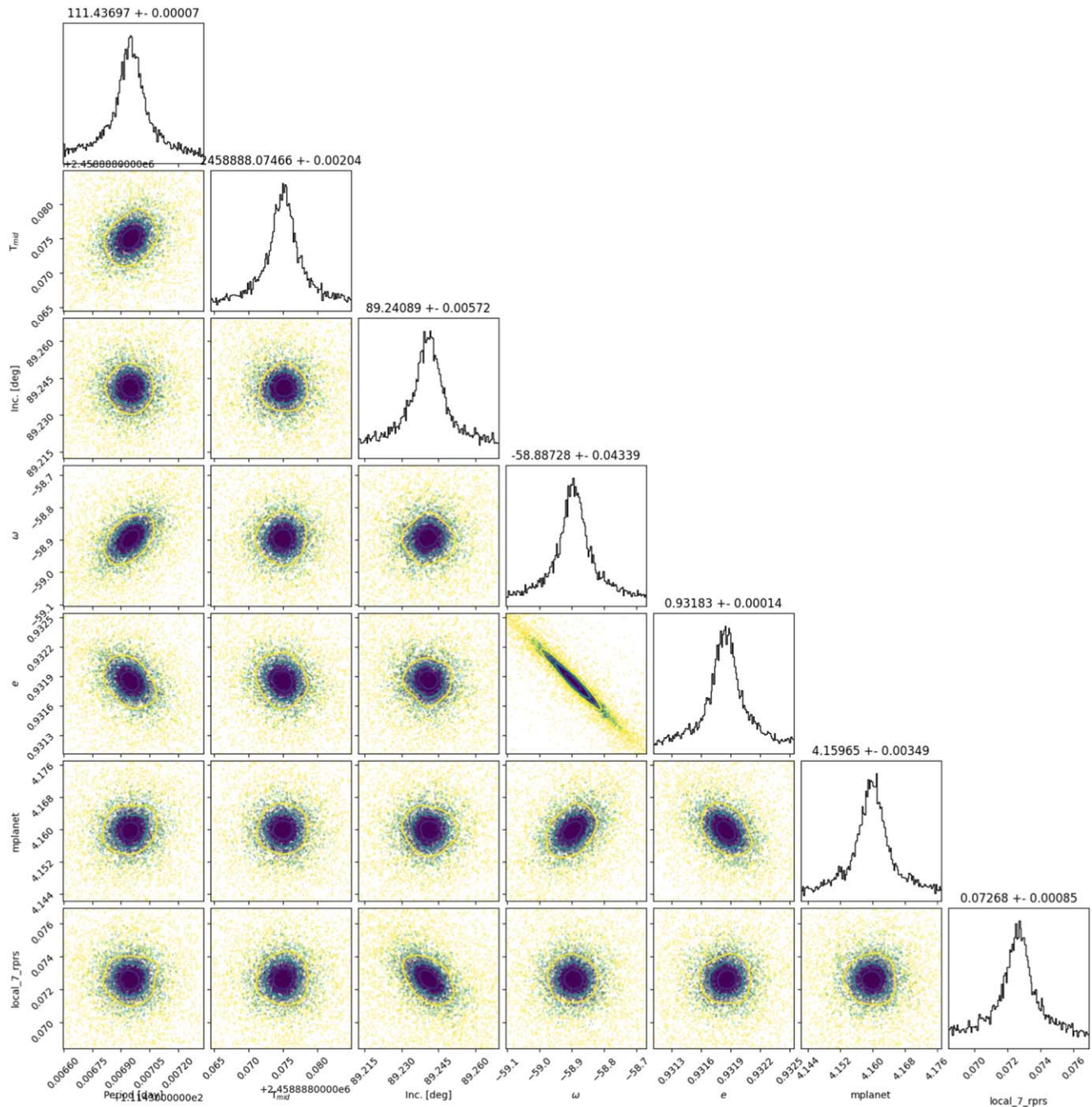









**Figure 9.** Posteriors for the joint fit between the radial velocity measurements, a transit light curve from TESS and historical measurements for midtransit and mideclipse. Measurements from Table 3 are included in an ephemeris estimate during the fitting process and added into the likelihood function. The best-fit radial velocity model can be found in Figure 4, the best-fit transit model is shown in Figure 1 and the final ephemeris is shown in Figure 6. The data points in each correlation plot are color coded to the likelihood, with darker colors representing higher likelihoods. The contours represent the  $N\sigma$  boundary using the uncertainty reported in each column's title.

### ORCID iDs

Kyle A. Pearson <https://orcid.org/0000-0002-5785-9073>  
 Charles Beichman <https://orcid.org/0000-0002-5627-5471>  
 B. J. Fulton <https://orcid.org/0000-0003-3504-5316>  
 Thomas M. Esposito <https://orcid.org/0000-0002-0792-3719>  
 Robert T. Zelle <https://orcid.org/0000-0001-7547-0398>  
 David R. Ciardi <https://orcid.org/0000-0002-5741-3047>  
 John Engelke <https://orcid.org/0000-0002-5977-5607>

Tamim Fatahi <https://orcid.org/0000-0002-0665-5759>  
 Arin Avsar <https://orcid.org/0000-0001-7801-7425>  
 Varun Bhalerao <https://orcid.org/0000-0002-6112-7609>  
 Alexandra D. Burnett <https://orcid.org/0000-0001-5248-1705>  
 Jennifer Burt <https://orcid.org/0000-0002-0040-6815>  
 Edward Gomez <https://orcid.org/0000-0001-5749-1507>  
 Bruno Guillet <https://orcid.org/0000-0003-4091-0247>  
 Tiffany Kataria <https://orcid.org/0000-0003-3759-9080>

Anastasia Kokori  <https://orcid.org/0000-0002-3205-0147>  
 Harsh Kumar  <https://orcid.org/0000-0003-0871-4641>  
 Georgios Lekkas  <https://orcid.org/0000-0003-3559-0840>  
 Alessandro Marchini  <https://orcid.org/0000-0003-3779-6762>  
 Nicola Meneghelli  <https://orcid.org/0000-0002-5105-635X>  
 Chow-Choong Ngeow  <https://orcid.org/0000-0001-8771-7554>  
 Subham Samantaray  <https://orcid.org/0000-0003-2167-9764>  
 Vishwajeet Swain  <https://orcid.org/0000-0002-7942-8477>  
 Kevin Wagner  <https://orcid.org/0000-0002-4309-6343>

## References

- Alonso, R. 2018, *Handbook of Exoplanets* (Berlin: Springer), 40  
 Blanchet, L., Hébrard, G., & Larrourou, F. 2019, *A&A*, **628**, A80  
 Bonomo, A. S., Desidera, S., Benatti, S., et al. 2017, *A&A*, **602**, A107  
 Buchner, J. 2017, arXiv:1707.04476  
 Buchner, J. 2021, *JOSS*, **6**, 3001  
 Butler, R. P., Marcy, G. W., Williams, E., et al. 1996, *PASP*, **108**, 500  
 Ciardi, D. R., Beichman, C. A., Horch, E. P., & Howell, S. B. 2015, *ApJ*, **805**, 16  
 de Wit, J., Lewis, N. K., Langton, J., et al. 2016, *ApJL*, **820**, L33  
 Dragomir, D., Harris, M., Pepper, J., et al. 2020, *AJ*, **159**, 5  
 Fabrycky, D. C. 2010, in *Exoplanets*, ed. S. Seager (Tucson, AZ: Univ. of Arizona Press), 217  
 Feroz, F., & Hobson, M. P. 2008, *MNRAS*, **384**, 449  
 Ford, E. B. 2005, *AJ*, **129**, 1706  
 Fossey, S. J., Waldmann, I. P., & Kipping, D. M. 2009, *MNRAS*, **396**, L16  
 Fulton, B. J., Petigura, E. A., Blunt, S., et al. 2018, *PASP*, **130**, 044504  
 Garcia-Melendo, E., & McCullough, P. R. 2009, *ApJ*, **698**, 558  
 Hébrard, G., Désert, J.-M., Díaz, R. F., et al. 2010, *A&A*, **516**, A95  
 Hippke, M., David, T. J., Mulders, G. D., et al. 2019, *AJ*, **158**, 143  
 Holman, M. J., & Murray, N. W. 2005, *Sci*, **307**, 1288  
 Huber, K. F., Czesla, S., & Schmitt, J. H. M. M. 2017, *A&A*, **597**, A113  
 Jenkins, J. M., Caldwell, D. A., Chandrasekaran, H., et al. 2010, *ApJL*, **713**, L87  
 Jenkins, J. M., Twicken, J. D., McCauliff, S., et al. 2016, *Proc. SPIE*, **9913**, 99133E  
 Jones, H. R. A., Butler, R. P., Tinney, C. G., et al. 2006, *MNRAS*, **369**, 249  
 Kasliwal, M. M., Cannella, C., Bagdasaryan, A., et al. 2019, *PASP*, **131**, 038003  
 Kokori, A., Tsirias, A., Edwards, B., et al. 2022, *ExA*, **53**, 547  
 Laughlin, G., Deming, D., Langton, J., et al. 2009, *Natur*, **457**, 562  
 Lewis, N. K., Parmentier, V., Kataria, T., et al. 2017, arXiv:1706.00466  
 Morello, G., Claret, A., Martin-Lagarde, M., et al. 2020, *AJ*, **159**, 75  
 Moutou, C., Hébrard, G., Bouchy, F., et al. 2009, *A&A*, **498**, L5  
 Naef, D., Latham, D. W., Mayor, M., et al. 2001, *A&A*, **375**, L27  
 Nesvorný, D., & Morbidelli, A. 2008, *ApJ*, **688**, 636  
 Pearson, K. A. 2019, *AJ*, **158**, 243  
 Pearson, K. A., Griffith, C. A., Zellem, R. T., et al. 2019, *AJ*, **157**, 21  
 Buchner, J. 2014, arXiv:1407.5459  
 Pont, F., Hébrard, G., Irwin, J. M., et al. 2009, *A&A*, **502**, 695  
 Ricker, G. R., Winn, J. N., Vanderspek, R., et al. 2015, *JATIS*, **1**, 014003  
 Rosenthal, L. J., Fulton, B. J., Hirsch, L. A., et al. 2021, *ApJS*, **255**, 8  
 Shporer, A., Winn, J. N., Dreizler, S., et al. 2010, *ApJ*, **722**, 880  
 Skilling, J. 2004, in *AIP Conf. Proc. 735, Bayesian Inference and Maximum Entropy Methods in Science and Engineering: XXIV International Workshop on Bayesian Inference and Maximum Entropy Methods in Science and Engineering* (Melville, NY: AIP), 395  
 Stassun, K. G., Collins, K. A., & Gaudi, B. S. 2017, *AJ*, **153**, 136  
 Tinetti, G., Drossart, P., Eccelston, P., et al. 2016, *Proc. SPIE*, **9904**, 1  
 Tsirias, A., Waldmann, I. P., Rocchetto, M., et al. 2016, *ApJ*, **832**, 202  
 Vogt, S. S., Radovan, M., Kibrick, R., et al. 2014, *PASP*, **126**, 359  
 Winn, J. N., Howard, A. W., Johnson, J. A., et al. 2009, *ApJ*, **703**, 2091  
 Wittenmyer, R. A., Endl, M., Cochran, W. D., & Levison, H. F. 2007, *AJ*, **134**, 1276  
 Wittenmyer, R. A., Endl, M., Cochran, W. D., Levison, H. F., & Henry, G. W. 2009, *ApJS*, **182**, 97  
 Zellem, R. T., Biferno, A., Ciardi, D., et al. 2019, *BAAS*, **51**, 3  
 Zellem, R. T., Pearson, K. A., Blaser, E., et al. 2020, *PASP*, **132**, 054401